Powder Technology 433 (2024) 119203

Contents lists available at ScienceDirect

Powder Technology

journal homepage: www.journals.elsevier.com/powder-technology

Experimental and computational investigations on mechanically alloyed $Fe_{55}Co_{30}Ni_{15}$ powders

Abdelkrim Houssou [a], Samia Amirat [a], Hana Ferkous [b,**], Safia Alleg [c], Karima Dadda [c], Rahima Boulechfar [d], Lakhdar Abadlia [e,f], Wahiba Bouchelaghem [e], Javed Khan Bhutto [g], Maha Awjan Alreshidi [h], Krishna Kumar Yadav [i,j], Noureddine Elboughdiri [l,m], Alessandro Erto [n], Yacine Benguerba [k,l,*]

[a] Laboratory of Nanomaterials-Corrosion and Surface Treatments, University Badji Mokhtar Annaba, Algeria
[b] Laboratory of Mechanical Engineering and Materials, Faculty of Technology, University of 20 Aout 1955, Skikda 21000, Algeria
[c] Laboratory of Magnetism and Spectroscopy of Solids (LM2S), Department of Physics, Badji Mokhtar University Annaba, 23000 Annaba, Algeria
[d] Laboratoire des matériaux et génie énergétique LMGE, Université 20 Août 1955, Skikda, Algeria
[e] Laboratory of Inorganic Materials Chemistry (LIMC), Badji Mokhtar-Annaba University, Annaba 23000, Algeria
[f] Department of Material Sciences, Faculty of Sciences and Technologies, University of Mohamed Cherif Messaadia, Souk-Ahras 41000, Algeria
[g] Department of Electrical Engineering, College of Engineering, King Khalid University, Abha, Saudi Arabia
[h] Department of Chemistry, University of Ha'il, Ha'il 81441, Saudi Arabia
[i] Faculty of Science and Technology, Madhyanchal Professional University, Ratibad, Bhopal 462044, India
[j] Environmental and Atmospheric Sciences Research Group, Scientific Research Center, Al-Ayen University, Thi-Qar, Nasiriyah 64001, Iraq
[k] Laboratoire de Biopharmacie et Pharmacotechnie (LBPT), Ferhat Abbas Setif 1 University, Setif 19000, Algeria
[l] Chemical Engineering Department, College of Engineering, University of Ha'il, P.O. Box 2440, Ha'il 81441, Saudi Arabia
[m] Chemical Engineering Process Department, National School of Engineers Gabes, University of Gabes, Gabes 6029, Tunisia
[n] Dipartimento di Ingegneria Chimica, deiMateriali e della Produzione Industriale, Università di Napoli Federico II, P.leTecchio, 80, 80125 Napoli, Italy

HIGHLIGHTS

- Successfully prepared nanostructured $xCoNi_{35-x}Fe$ powders.
- Cubic crystalline structure was observed by XRD, SEM and VSM investigations.
- Nanostructured $Fe_{65}Ni_{30}Co_5$ alloys have been produced using the MA method.
- A study of the magnetization in relation to the applied magnetic field was conducted.

GRAPHICAL ABSTRACT

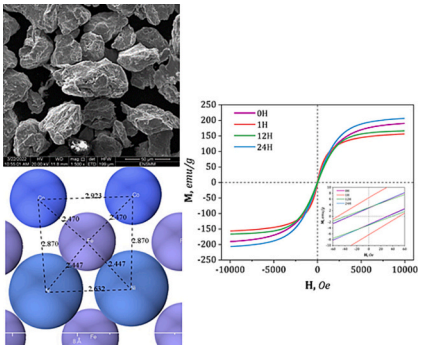

* Corresponding author at: Laboratoire de Biopharmacie et Pharmacotechnie (LBPT), Ferhat Abbas Setif 1 University, Setif 19000, Algeria.
** Corresponding author.
E-mail addresses: h.ferkous@univ-skikda.dz (H. Ferkous), yacinebenguerba@univ-setif.dz (Y. Benguerba).

https://doi.org/10.1016/j.powtec.2023.119203
Received 16 August 2023; Received in revised form 6 November 2023; Accepted 23 November 2023
Available online 3 December 2023

ARTICLE INFO

Keywords:
Mechanical alloying
Microstructure
Magnetic properties
Hyperfine structure

ABSTRACT

Nanocrystalline $Fe_{55}Co_{30}Ni_{15}$ powder alloy was created via mechanical alloying in a planetary ball mill (Fritsch P7) under an argon atmosphere. Structural, microstructural, and magnetic features were analyzed using X-ray diffraction (XRD), scanning electron microscopy (SEM) with energy-dispersive X-ray spectroscopy (EDX), and vibrating sample magnetometry (VSM). The results indicated a coexistence of body-centered cubic (BCC) and face-centered cubic (FCC) solid solutions, with BCC being predominant (96%) and displaying an average grain size of 11 nm. Both BCC and FCC phases exhibited a significant density of dislocations ($\sim 10^{16}$ per square meter). The powder alloy demonstrated soft magnetic behavior with a saturation magnetization of 206.5 emu/g and a coercivity of 32.63 Oe, indicative of multidomain properties based on the Mr./Ms. ratio. Theoretical analysis confirmed precise computational simulation parameters at room temperature.

1. Introduction

Magnetization is a defining feature of the pure transition metals Fe, Co, and Ni, making them highly sought-after materials with a wide array of applications [1,2]. Consequently, alloys based on Fe, Co, and Ni exhibit exceptional magnetic properties, enabling the development of hard, soft, and semi-hard magnetic materials. Among these, iron-nickel (Fe-Ni) alloys have gained significant attention in various industries, particularly for their utilization as soft-magnetic materials. Key characteristics of these materials include narrow hysteresis loops, low coercive force, high saturation induction, excellent permeability, and corrosion resistance [3–5].

By combining the elements Fe, Co, and Ni, it is possible to engineer materials with desirable structural, microstructural, mechanical, thermal, and magnetic attributes. Ternary Fe-Co-Ni alloys, in particular, have garnered substantial interest due to their unique properties and their wide range of applications in aerospace, automotive, electronics, and other industries. Researchers have explored numerous compositions of Fe-Ni-Co alloys by adjusting the ratios of Fe, Ni, and Co to optimize their properties, leading to the creation of materials suited for magnetic recording, microwave absorption, high strength, and corrosion resistance [6–16].

In materials science, the synthesis conditions play a pivotal role in determining material properties. Nanocrystalline (NC) Fe-Ni-Co alloys have been produced using various techniques, including electrodeposition, sol-gel, chemical reduction methods, hydrogen reduction, and mechanical alloying (MA) [7,11–16]. Among these techniques, MA stands out as an economical and straightforward method for crafting solid solutions, intermetallic compounds, amorphous and nanocrystalline alloys, high-entropy alloys, and supersaturated solid solutions with tailored magnetic, electrical, mechanical, and thermal characteristics [17–23]. MA is a solid-state reaction that relies on repeated processes like fracture, cold welding, agglomeration, and de-agglomeration of powder particles, typically starting from elemental powders or pre-alloyed materials. The final product's properties are influenced by factors such as the composition and nature of the initial powders, milling parameters like the type of ball mill, ball-to-powder weight ratio (BPR), milling time, atmosphere, control agents, milling media, and milling speed.

As an example, nanocrystalline $Fe_{50}Co_{50} - xNi_x$ (x = 10, 20, 40, and 50) alloys were synthesized through a hydrazine reduction process with PVP [7]. These powders exhibited a wide size distribution, and their magnetic properties varied with the transition from a body-centered cubic (BCC) to a face-centered cubic (FCC) structure as the Ni content increased. Similarly, NC $Fe_xNi_{80-x}Co_{20}$ (x = 20, 30, 40, 50) materials prepared using a chemical reduction method displayed an FCC crystal structure with lattice parameters in the range of 3.546–3.558 Å, crystallite sizes between 22.8 and 27.5 nm, coercivity values ranging from 122 to 170 Oe, and a significantly lower saturation magnetization of 41.2–54.3 emu/g [8]. Milling Ni40Fe30Co30 powders led to the formation of a single FCC crystal structure (a = 3.580 Å) after 9 h of milling, resulting in mean particle and grain sizes of about 4 μm and 8 nm, respectively. The coercivity and saturation magnetization were approximately 2.40 kA/m and 130.8 emu/g, respectively [24]. Spark plasma sintering (SPS) was employed to fabricate (Ni-21Fe) − xCo (x = 10, 20, 30, and 40) samples from milled powders, leading to a wide range of structural, magnetic, and mechanical properties[25]. The samples with higher Co content exhibited the highest Ms., Hc, Curie temperature, and hardness. In another approach, three distinct Ni-Co-Fe coatings were electrodeposited, displaying a single FCC structure with crystallite sizes between 8 and 12 nm and equiaxed grains. These coatings, characterized by high hardness (Hv = 4.2 GPa), low coercivity (Hc = 23 Oe), and excellent corrosion resistance, hold great promise for applications in microelectromechanical systems (MEMS) [26].

Theoretical studies are indispensable for understanding the mechanisms governing the macroscopic properties of materials and for predicting novel compounds and their characteristics. Contemporary computational approaches based on density functional theory (DFT) have become invaluable tools for researchers and scientists. Owing to its effectiveness and precision, DFT has become a prominent technique for characterizing and forecasting the attributes of nanomaterials [27–29]. The current study's objective is to explore the influence of milling time on the phase formation, microstructure, and magnetic properties of milled Fe55Co30Ni15 powders, with an additional focus on the electronic density of state (DOS) structure and magnetic state.

2. Experimental

To create the $Fe_{55}Co_{30}Ni_{15}$ (wt%) alloy, high-purity powders of cobalt (> 99.9%), nickel (> 99.9%), and iron (> 99.9%) were carefully blended. The milling process took place in a Fritsch P7 planetary ball mill using stainless steel balls and vials within an argon environment, all at room temperature. The rotation speed was set at 400 rpm, and the ball-to-powder weight ratio (BPR) was approximately 18:1. To prevent excessive temperature increase within the vials, the milling process was conducted for half an hour with intervals of a quarter of an hour for breaks. To assess the crystal structure of the mechanically alloyed powders, a PANalytical Empyrean X-ray diffractometer (XRD) was employed. The XRD was configured in a (θ-θ) Bragg Brentano geometry, utilizing Cu-Kα radiation (λ = 1.540598 Å) with a scanning range spanning 30 to 90° and a step size of 0.013°. The morphological characteristics of the powder were examined using scanning electron microscopy (FEI Quantum 250, SEM) equipped with energy-dispersive X-ray spectroscopy (EDX).

Furthermore, magnetic parameters, including saturation magnetization (Ms), coercivity (Hc), remanence (Mr), and the saturation to remanence ratio (Mr/Ms), were determined using a vibrating sample magnetometer (Lakeshore Model 7404). These measurements were conducted in the presence of an external magnetic field of 20 kOe at room temperature.

Finally, the Rietveld powder structure refinement was carried out using the MAUD program, which is based on the Rietveld method. This detailed analysis allowed for a precise characterization of the alloy's crystal structure [30–32].

3. Computational investigation

3.1. Theoretical model

In the simulations, the crystal structure employed belonged to the Fm-3 m space group, featuring the following lattice parameters: a = b = c = 3.5450 Å. To carry out these simulations, the Cambridge Arrayed Simulated Terahertz Energy Package (CASTEP) program was employed [33]. The exchange-correlation energy was computed using the GGA-PBE functional [33–36]. An ultra-soft pseudopotential (PP) approximation was adopted to represent the Optimized Troullier-Martins Functional (OTFG) set. This approach reduces the number of basis sets required to describe real electronic functions, effectively approximating the behavior of the atomic nucleus and core electrons. The valence electron configurations for the three elements are as follows: Fe: 3d6 4 s2, Ni: 3d8 4 s2, and Co: 3d7 4 s2. The analysis of the Brillouin region was conducted using the Monkhorst-Pack technique [37]. In calculations based on first principles, the energy of the ground state is a crucial quantity [38], and it is influenced by the sampling of the Brillouin zone and the energy cut-off. In this case, an energy cut-off of 440 eV was selected, and the k-points were adjusted accordingly to accommodate this new value. This arrangement was found to provide excellent stability and convergence for the simulations.

4. Results and discussion

4.1. Particles morphology

Mechanical alloying (MA) has a profound impact on the morphology of particles that have undergone substantial plastic deformation [39]. Fig. 1 presents scanning electron microscopy (SEM) images of both the initial and milled powder mixtures, showcasing the development of distinct particle shapes and sizes. The starting elements exhibit varying characteristics: Co powders have a spherical shape and particle sizes in the range of 61–149 μm, Fe particles display an irregular shape with a narrow size distribution (20–60 μm), and Ni powders are typically flake-like and agglomerate in sizes <10 μm. During the milling process, the balance between fracturing and cold welding hinges on the nature of the initial powders and has a substantial impact on material properties.

Nickel, iron, and cobalt metals are known for their moderate ductility and relative malleability, which means they can undergo shaping through severe plastic deformation without fracturing. Initially, during the first hour of milling, agglomerates and large particles with irregular shapes and sizes are formed. This stage is dominated by the cold welding process due to the malleability and ductility of Fe, Ni, and Co powders. The high contact pressure between the balls and powders, as well as between the balls and vials, leads to the creation of new surfaces that come into contact with one another under significant plastic deformation. This results in the flattening of the powder particles and the emergence of a layered morphology. Continued milling leads to a combination of continuous fracturing and cold welding processes, resulting in aggregates of smaller particles with irregular shapes and particle sizes ranging from 10 to 150 μm after 12 h of milling. As the milling time progresses and the applied stress surpasses the strength of the powder mixture, the powders undergo further fracturing, leading to the formation of smaller particles in the range of 3–30 μm after 24 h of milling. Additionally, the powder particles exhibit irregular and flattened morphologies. The achieved particle size distribution is a result of the intricate interplay between the fracturing and cold welding phenomena. The elemental composition of the 24-h milled powders was determined through EDX analysis, providing valuable insights into the composition of each particle. The EDX spectra, as depicted in Fig. 2, confirm that every particle contains the constituent elements (Fe, Co, and Ni) without any contamination from the milling media or the surrounding atmosphere. Notably, the elemental composition appears to be highly homogeneous, whether analyzed over a wide area (Fig. 2a) or a smaller region (Fig. 2b). The compositional analysis reveals minor variations in the content of the three elements: Fe content ranges slightly from 72.25 to 73.29 wt%, Co content falls within the range of 7.80 to 8.85 wt% and Ni content fluctuates between 17.86 and 19.95 wt%. It is worth noting that distinguishing between Ni and Co in the EDX spectra can be challenging, as their energy lines are very close to each other. Consequently, the resulting alloy could be described as a pseudo-binary Fe73(CoNi)27 alloy, considering the close alignment of Ni and Co in the compositional range.

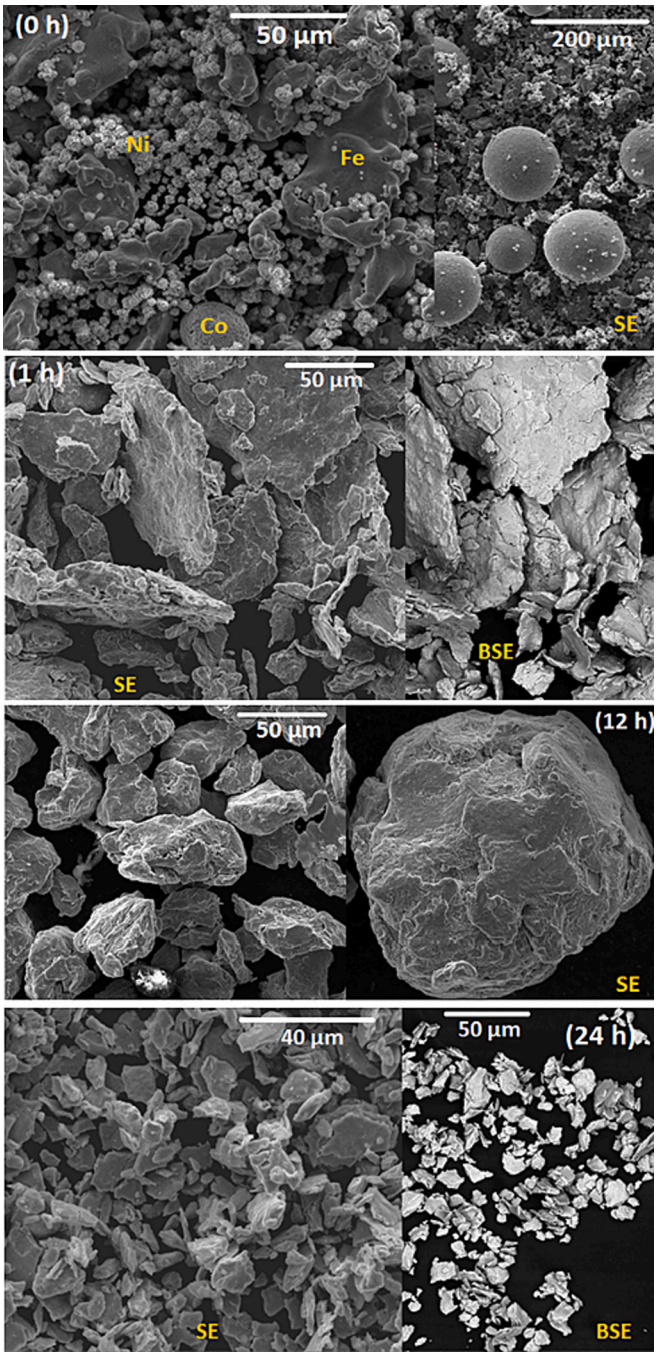

Fig. 1. Typical secondary electrons (SE) and backscattered electrons (BSE) SEM images of the starting and mechanically alloyed powders for 1, 12, and 24 h with different magnifications.

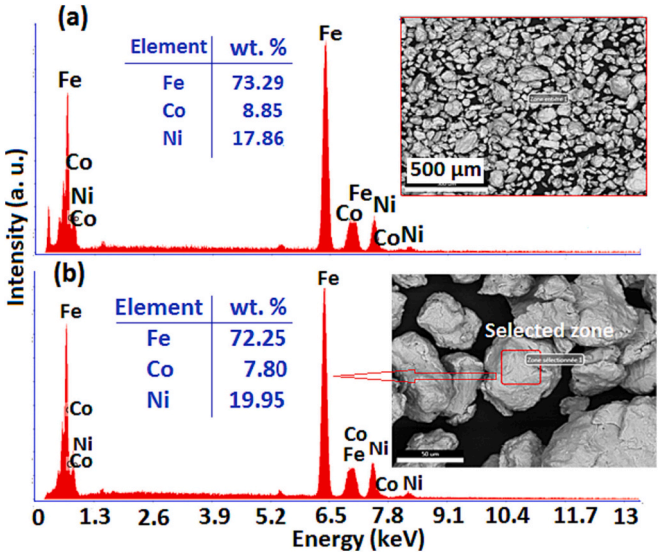

Fig. 2. EDX spectra and elemental analyses (insets) of the mechanically alloyed $Fe_{55}Co_{30}Ni_{15}$ powders for 24 h. The analyzed zone is shown in the insets.

4.2. X-rays diffraction analysis

The XRD patterns of the initial (0 h) and mechanically alloyed powders mixture are presented in Fig. 3. The initial mixture exhibits distinct characteristic peaks corresponding to the constituent elements: BCC Fe (space group Im-3 m, lattice parameter a0 = 2.8665 Å, ICSD file No: 9008536), FCC Co (space group Fm-3 m, lattice parameter a0 = 3.5441 Å, ICSD file No: 9012949), and FCC Ni (space group Fm-3 m, lattice parameter a0 = 3.516 Å, ICSD file No: 9009862). It is worth noting that the diffraction peaks of Co and Ni are challenging to distinguish from each other due to their similar crystal structures. The three constituent elements, Fe, Ni, and Co, are transition metals that belong to the same period (4th period) of the periodic table. They have nearly identical values of atomic radii (r_{Fe} = 0.124 nm, r_{Co} = 0.125 nm, and r_{Ni} = 0.125 nm), which allows for the substitution of one element with another without causing significant alterations in the crystal lattice. Furthermore, the formation of solid solutions is facilitated by the negative enthalpies of mixing ($\Delta H_{mix\ Fe\text{-}Co} = -1$ kJ/mol, $\Delta H_{mix\ Fe\text{-}Ni} = -2$ kJ/mol, and $\Delta H_{mix\ Co\text{-}Ni} = 0$ kJ/mol) [40].

After 1 h of milling, the characteristic diffraction peaks (111) and (011) of the initial elements overlap, but the (200), (002), (220), (112), and (022) peaks remain distinguishable. These diffraction peaks exhibit a significant reduction in intensity and a slight broadening. As the milling time progresses, the diffraction peaks undergo pronounced broadening and a reduction in intensity due to microstructure refinement and the introduction of various structural defects (such as vacancies, dislocations, grain boundaries, stacking faults, etc.) resulting from extensive plastic deformation. At 12 h of milling, the elemental Ni and Co peaks largely become indistinguishable, and only the peaks for the BCC Fe(Co, Ni) and FCC Co(Ni, Fe) solid solutions at around 44.68° and 43.74°, respectively, are observed. This indicates the mixing of the elemental powders at the atomic level. The slight shift in the peak positions to lower angles concerning the Fe (110) and Co (111) after 12 h of milling suggests that the mechanochemical reaction between the starting elements led to the formation of BCC and FCC solid solutions. This is because mechanical milling favors the first-order strains acting on a macroscopic scale by modifying the lattice parameter. Furthermore, the shift in peak positions is attributed to the partial substitution of Fe atoms by other transition metal atoms such as Co or Ni, as well as the partial substitution of Co atoms by Fe and Ni atoms. Accordingly, Rietveld refinement of the XRD patterns was conducted using BCC Fe, FCC Co, and FCC Ni phases for 1 h of milling, and Fe-based BCC Fe(Co, Ni) and Co-based FCC Co(Fe, Ni) solid solutions for 12 and 24 h of milling (see Fig. 4). The crystal structure, the average crystallite size (<L>), weight fraction, and root-mean-square (r.m.s.) microstrains ($<\sigma^2>^{1/2}$) are summarized in Table 1. The crystallite sizes of the initial Fe, Ni, and Co elements exhibited a significant reduction from 152 to 370 nm to approximately 42–113 nm after one hour of milling. As milling time increased, the crystallite size reached 11 nm and 20 nm after 24 h of milling for the BCC and FCC solid solutions, respectively, while lattice strains increased to 0.45% and 0.20%.

Notably, this result contrasts with that obtained for the ball-milled Fe50Ni15Co30 powder, which had a lower crystallite size for the FCC solid solution (~10 nm) compared to the BCC solid solution (~15 nm)

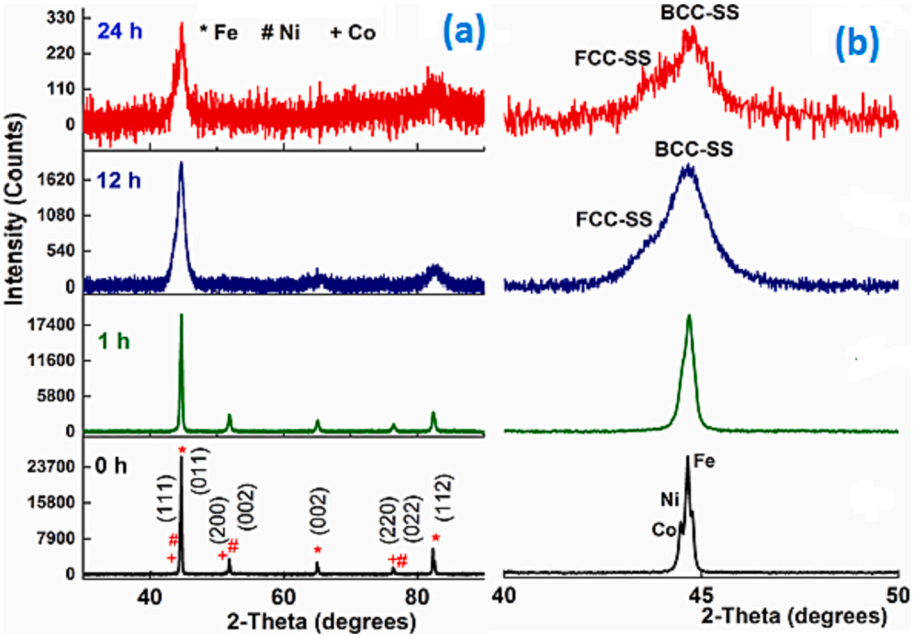

Fig. 3. XRD patterns of the mechanically alloyed powders as a function of milling time (a), and the evolution of the main diffraction peak during the milling process (b).

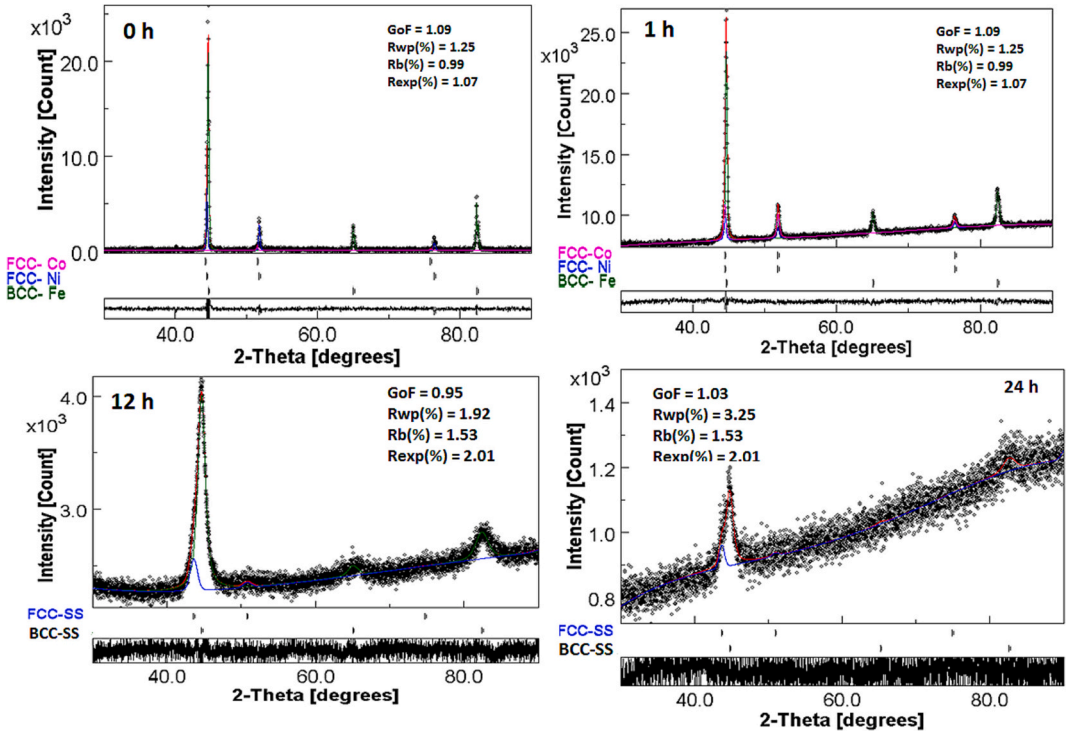

Fig. 4. Rietveld refinement of the XRD patterns of the un-milled and milled powders for 1 h, 12 h, and 24 h. Experimental (dots), calculated (line), and difference patterns (down) are displayed. Diffraction line positions of the identified phases are illustrated as small markers (|). GoF, Rwp, Rb, and Rexp are given in insets.

Table 1
Crystal structure, weight fraction (%), lattice parameter (a), relative deviation (Δa), average crystallite size ($<L>$), and average lattice strain, ($<\sigma^2>^{1/2}$) of the milled $Fe_{0.55}Ni_{0.15}Co_{0.3}$ powders.

Milling time (h)	Phases	Weight fraction (%) ± 1	(a) (Å) ± 10^{-4}	Δa (%)	($<L>$) ± 2 (nm)	$<\sigma^2>^{1/2}$ (%) ± 10^{-2}
0	BCC-Fe	57.25	2.8665	–	204	0.002
	FCC-Ni	10.8	3.5248	–	370	0.004
	FCC-Co	31.95	3.5441	–	152	0.004
1	BCC-Fe	71.5	2.8653	−0.052	113	0.005
	FCC-Ni	9.3	3.5229	−0.053	80	0.005
	FCC-Co	19.2	3.5228	−0.6	42	0.004
12	BCC-SS	94.8	2.866	−0.017	12	0.51
	FCC-SS	5.2	3.5899	1.292	40	0.89
24	BCC-SS	96	2.8619	−0.16	11	0.45
	FCC-SS	4	3.5855	1.168	20	0.2

after 30 h of milling with a milling speed of 400 rpm and a BPR of 10:1 [41]. The crystallite size, <L>, and r.m.s. microstrains, $<\sigma^2>^{1/2}$, were utilized to calculate the mean dislocation density using the following Eq. [42]:

$$\rho_{dis} = 2\sqrt{3}\,(\sigma^2)^{1/2} \Big/ (\langle L > x\,\beta) \quad (1)$$

where β is Burger's vector describing the direction and magnitude of lattice distortions. It equals $a\sqrt{3}/2$ for the BCC structure and $a\sqrt{2}/2$ for the FCC structure. At the outset of milling (1 h), the dislocation density values for Fe (6.10^{14} m^{-2}), Co (1.10^{15} m^{-2}), and Ni (8.10^{14} m^{-2}) are intermediate between those of screw (~10^{13} m^{-2}) and edge dislocations (~10^{16} m^{-2}), which can be generated by plastic deformation [43]. Consequently, the dislocations generated during the milling process may represent a mixture of edge and screw dislocations. After 24 h of milling, the values of the density of dislocations are in the same order of magnitude as that of edge dislocations for both the BCC (57.10^{16} m^{-2}) and FCC (14.10^{16} m^{-2}) solid solutions. The higher density of dislocations in the mechanically alloyed powders facilitates the formation of the solid solution by enhancing atomic diffusion at room temperature. Similar results were obtained for the 24-h milled $Fe_{50}Co_{50}$ [44], 20-h milled $Fe_{60}Al_{40}$ [45], and 20-h milled FeCoNi alloys [46]. In the case of the $Fe_{50}Co_{25}Ni_{25}$ powders milled for 100 h, the calculated dislocation density was approximately $\rho = 1.25 \times 10^{15}$ m^{-2} [47].

The lattice parameters of the Fe, Co, and Ni elements decrease after the first hour of milling to approximately 2.8653 ± 10^{-4} Å, 3.5228 ± 10^{-4} Å, and 3.5229 ± 10^{-4} Å, respectively. The relative change in the size of the unit cell of a crystal lattice can be quantified by the relative deviation, which represents the difference in the cell parameter (a) compared to a reference value (a_0). This can be expressed using the equation $\Delta a\ (\%) = (a - a_0) / a_0$, where a_0 and a are the lattice parameters from the ICSD file and for a given milling time, respectively. Consequently, the relative deviation reaches as much as −0.052%, −0.053%, and − 0.60% for Fe, Ni, and Co, respectively. The contraction of the crystal lattice is a result of the heavy plastic deformation of the powder particles and the introduction of several structural defects during the milling process. The most significant relative deviations are observed for the FCC Co compared to those of BCC Fe and FCC Ni, and this may be attributed to stacking faults. In the case of the new BCC solid solution, the lattice parameter is lower than that of pure Fe, deviating by approximately −0.017% and − 0.16% for the milled powders after 12 h and 24 h, respectively. However, the lattice parameter of the new FCC solid solution increases to about 3.5899 Å and 3.5855 Å after 12 h and 24 h of milling compared to that of Co, resulting in relative deviations of

about −1.292% and − 1.168%, respectively. These variations in lattice parameters are indicative of the changes in the crystal structure and composition resulting from the mechanical alloying process. The small fluctuations in the weight fractions of the elemental powders compared to the nominal composition may be attributed to the heterogeneity of the analyzed powder mixture. Notably, there is an increase in the weight percent of BCC Fe to approximately 71.5%, and this increase comes at the expense of the weight fractions of Ni (9.3%) and Co (12.2%). This increase can be attributed to the diffusion of both Co and Ni into the Fe matrix. This assumption is consistent with the observed formation of agglomerates in the SEM images. The weight fraction of the BCC solid solution reaches 94.8% after 12 h of milling and then stabilizes at around 96% after 24 h of milling. Since Fe and Co are miscible over the entire concentration range, the predominance of the BCC solid solution is primarily a result of the diffusion of Co atoms into the Fe lattice. It's worth noting that the diffusion of Co atoms into the Fe lattice occurs faster than that of Ni atoms. Additionally, in Fe-Co alloys, Fe atoms can be substituted with Co atoms, which leads to a decrease in the lattice parameter, aligning with the findings reported in Table 1.

Different results have been obtained for the Fe-Co-Ni system depending on the conditions of the manufacturing route (composition, ball mill type, BPR, milling time, etc.). For example, the end product of the ball milled $Fe_{50}Co_{40}Ni_{10}$ (wt%) for 90 h in the planetary ball mill QM-3SP4 with a BPR of 15:1 and a rotation speed of 320 rpm consisted of a single BCC Fe(Co, Ni) solid solution [48]. The Crystal structure of the milled $Fe_{50}Co_{30}Ni_{20}$ (wt%) powders for 30 h in a high energy planetary mill using a BPR of 10:1 and a rotation speed of 400 rpm was a mixture of 65.64% BCC solid solution ($a = 2.867$ Å, $<L \geq 18.6$ nm) and 35.74% FCC solid solution ($a = 3.535$ Å, $<L \geq 7.6$ nm) [41].

4.3. Magnetic characteristics

The effect of severe plastic deformations (SPD) during the milling process can be examined by microstructural analysis and magnetic properties (Hc, Ms., Mr./Ms) measurements to establish quantitative relationships between them. Nonetheless, the exact quantitative relationship may vary depending on the unique properties of the material, the type of deformation, and the experimental setup used. Fig. 5 shows the magnetization response of the mechanically alloyed powders to changes in the applied magnetic field (M-H) at room temperature. The hysteresis loops are narrow and exhibit a sigmoidal shape characteristic of soft magnetic materials. The evolutions of the saturation magnetization, coercivity, remanence, and squareness ratio as a function of milling time are exposed in Fig. 6.

The saturation magnetization exhibits a two-stage behavior against

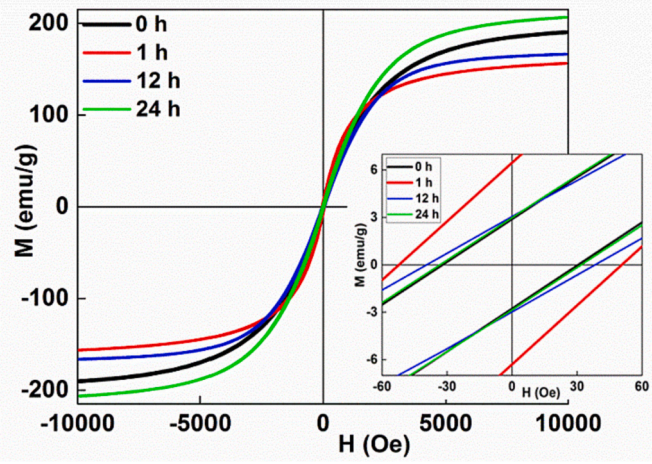

Fig. 5. Field dependence of magnetization for the initial and milled powders for 1, 12, and 24 h. The inset shows the enlargement of the central part.

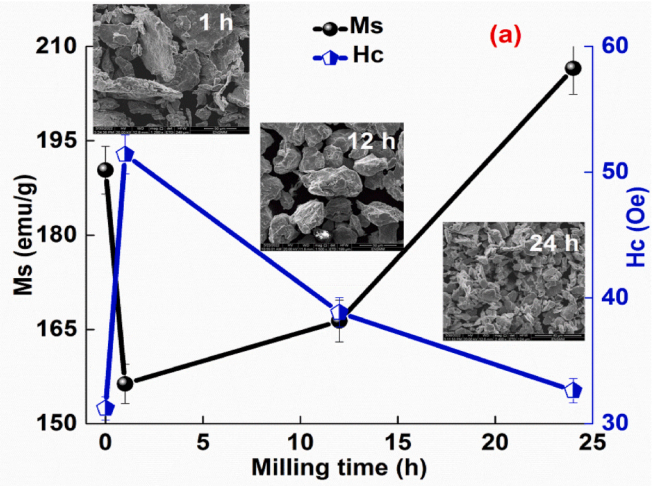

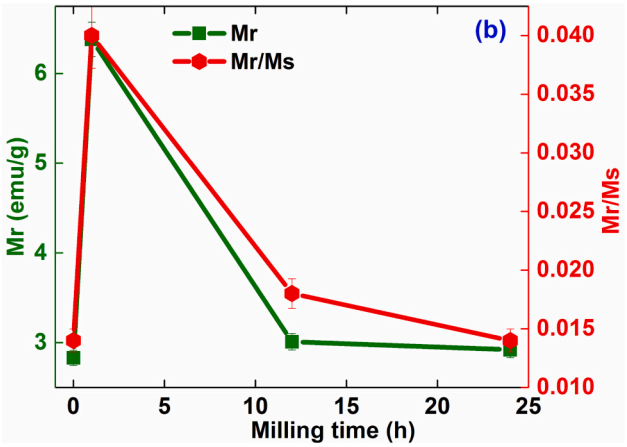

Fig. 6. (a) Evolution of Ms. and Hc versus milling time, and typical morphologies of the powder particles are shown in insets, and (b) variation of Mr. and Mr./Ms. with milling time.

the milling time (Fig. 6a). Ms. drops from 190.34 emu/g for the initial mixture to 156.34 emu/g after 1 h of milling and then rises to 166.34 emu/g and 206.50 emu/g after 12 h and 24 h of milling, respectively. The saturation magnetization can be affected by several factors such as the crystal structure, atomic and electronic structure, temperature, impurities and defects, etc. The decrease in Ms. during the initial stage of milling may be due to crystalline defects and the decrease in the lattice parameters of the magnetic Fe, Co, and Ni elements in good agreement with the XRD results. Besides, mechanical strains may lead to the reduction in Ms. because they alter the crystal structure and affect the interatomic distances and the arrangement of magnetic domains. The effect of mechanical strains is supported by the morphology of the powder particles that experience severe deformation and flattening after 1 h of milling (Fig. 1). The subsequent rise in Ms. after 12 h and 24 h of milling is due to the gradual formation of the Fe-Co-Ni alloy through the dissolution of Ni and Co atoms in the Fe matrix and the development of the Fe(Ni, Co) BCC solid solution as Fe, Co, and Ni promote strong magnetic interactions between neighboring atoms, leading to higher Ms. values. The increase in Ms. might also be related to the atomic disorder and the change in the nearest-neighbor configuration of magnetic atoms. The magnetic moment of Fe atoms depends on their local environment, while that of Co atoms does not. The estimated magnetic moment values are about 2.049 μ_B, 1.683 μ_B, 1.791 μ_B, and 2.223 μ_B for the 0 h, 1 h, 12 h, and 24 h, respectively. The decrease of the magnetic moment at the beginning of milling can be associated with the contraction of the crystal lattice owing to the SPD. However, the increase in the magnetic moment

from 12 h of milling can be due to the solid solution formation via the substitution of Fe atoms by Co atoms because the magnetic moment of the Co atoms (1.70 μ_B) is higher than that of the Ni atoms (0.6 μ_B).

Different Ms. values were obtained depending on the preparation conditions. The obtained Ms. value of 206.5 emu/g after 24 h of milling is lower than those reported for the ball-milled pure Fe (Ms = 213 emu/g) and $Fe_{50}Co_{50}$ powders (Ms = 215 emu/g) for 40 h [49]. The Ms. = 206.5 emu/g is higher than that obtained for the mechanically alloyed $Fe_{50}Ni_{10}Co_{40}$ powders using a BPR of about 15:1 and a rotation speed of 320 rpm with a maximum value of 153 emu/g after 25 h and a reduction to about 134 emu/g after 90 h milling [48]. The synthesized NC $Fe_{50}Ni_{30}Co_{20}$ powders ($L = 23$ nm) using a chemical reduction technique exhibited a lower Ms. value of 41 emu/g in comparison to that obtained for the same composition prepared by MA (Ms = 145 emu/g) [48].

The coercivity measures the material's ability to resist magnetization. The coercivity of ball-milled powders originates from several factors, such as composition, crystallite size, internal strains, impurities, dislocations, non-spherical shapes, and surface irregularities. The increase in coercivity (Fig. 6a) at the beginning of the milling time (1 h) to Hc = 51.42 Oe can be due to the plastic deformation effect, accumulation of internal stresses, and high levels of structural defects. Plastic deformation caused by mechanical stress during the milling process can have a significant impact on the behavior of the magnetic domain walls and, thus, on the overall magnetic properties. Plastic deformation refers to a permanent and irreversible change in the shape and structure of the material, which is visible in the SEM image (Fig. 1a, h). Dislocations, grain boundaries, and stacking faults can serve as pinning sites for magnetic domain walls, affecting their immobilization, hindering their movement, and increasing coercivity. The reduction in Hc to about 32.63 Oe after 24 h of milling can be mainly due to the decrease in the crystallite size (Table 1) in agreement with the random anisotropy model [50].

The Mr./Ms. ratio and Mr. exhibit the same tendency as a function of milling time (Fig. 6b). The Mr./Ms. ratio can be affected by microstructure change in the mechanically alloyed powders. Remanent magnetization indicates the stored magnetization in magnetic materials even after the external magnetic field removal. However, the Mr./Ms. ratio defines the degree of squareness of the hysteresis loop of a magnetic material by providing information about how well the material retains its magnetization when an external magnetic field is applied and removed. It is an insightful criterion for assessing the domain state, distinguishing between single domains (Mr/Ms. > 0.5) and multi-domains (Mr/Ms. < 0.1). The Mr./Ms. values (< 0.1) indicate that the powder particles are multi-domains where the magnetization modification can be due to the domain wall movement in relatively low fields.

4.4. Theoretical study

Initially, the first crystal structure space group was chosen to represent the Fe-Ni-Co phase. After several cycles, the convergence limit of 5.10^{-6} eV/atom was attained. The experimental results show that the lattice parameters at room temperature are $a = b = c = 2.8660$ Å. The calculated $a = b = c = 2.8664$ Å value is close to these values. These data demonstrate that the computational simulation's fundamental structure was successfully chosen (Fig. 7). The X-Pert program found a compound with the same formula $Fe_{55}Co_{30}Ni_{15}$.

Analyzing the samples' electronic characteristics was done using the electronic density of states (DOS). Fig. 8a shows the total DOS of the $Fe_{55}Co_{30}Ni_{15}$ alloy. From −10 to 20 eV, the DOS's most significant peaks may be seen. Fig. 8a depicts $Fe_{55}Co_{30}Ni_{15}$ with a clear up/down electron spin separation, demonstrating the material's ferromagnetic properties. Fig. 8b illustrates the peak in spin-up for the Fe 3d state. The 3d orbitals of Fe, Ni, and Co predominate in the conduction band.

According to Pauli's exclusion principle, the difference between the conduction electron populations' spin-up and spin-down plays a key role in controlling charge density. Measuring a crystal's spin density as the number of electrons per cubic meter is possible. The difference between electrons spinning up and down is equivalent to the crystal cell's integral value in a mathematical sense.

The integration of "integrated spin densities"—the total amount of electrons in a material provides a qualitative estimate of magnetic ordering. The magnetic state may be determined by comparing this value to the absolute magnitude in Table 2 [51]. Bohr magnetons (BMs) are used to calculate the magnetic dipole moment. Integrated spin density (ISD) values of 43.7681 and 47.2576 BM indicate that the material is ferromagnetic. As seen in Fig. 9 the Fe atoms' spin-up state in $Fe_{55}Co_{30}Ni_{15}$ results in a weak magnetic field.

5. Conclusion

In this study, we conducted a comprehensive investigation of the mechanical alloying process to synthesize nanocrystalline $Fe_{55}Co_{30}Ni_{15}$ powders. Various characterization techniques, including X-ray diffraction (XRD), scanning electron microscopy (SEM), energy-dispersive X-ray spectroscopy (EDX), and vibrating sample magnetometry (VSM), were employed to examine the structural, microstructural, elemental composition, and magnetic properties of the material during different stages of milling. The XRD analysis unveiled the transformation of the material into a coexistence of body-centered cubic (BCC) and face-centered cubic (FCC) solid solutions after 24 h of milling, with BCC as the dominant phase. The microstructural analysis demonstrated a significant reduction in crystallite size, with the FCC and BCC phases

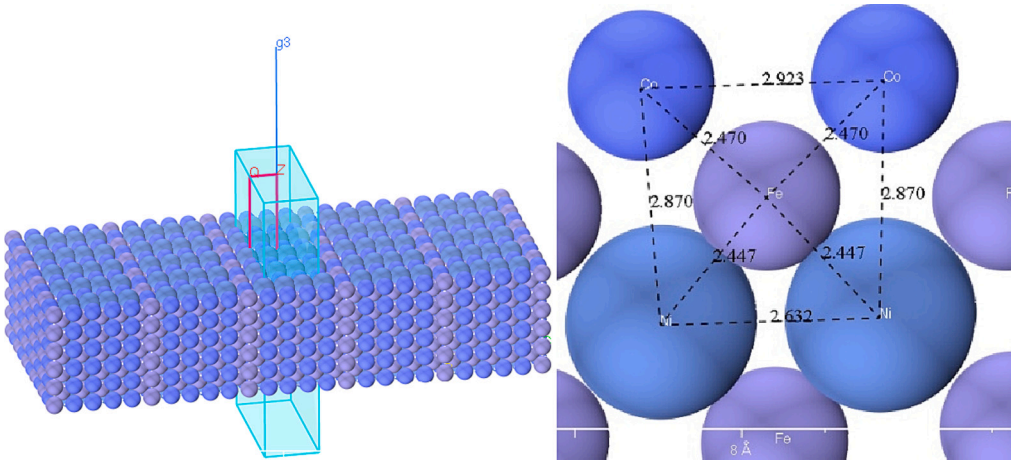

Fig. 7. Representation of the optimized structure.

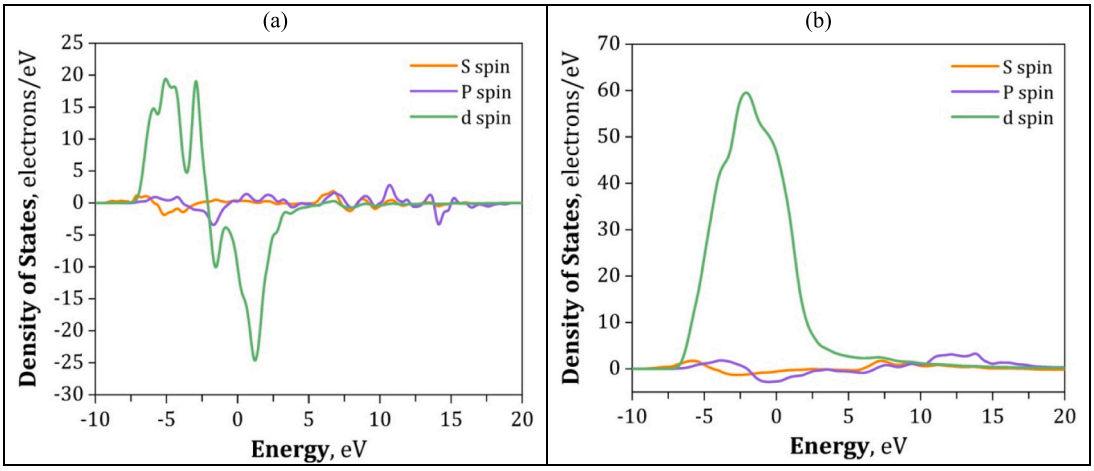

Fig. 8. Calculated PDOS for the $Fe_{55}Co_{30}Ni_{15}$ structure: (a) DOS, and (b) integrated DOS.

Table 2
The simulated crystal unit cell's magnetic ordering.

Parameter	Ferromagnetic	Paramagnetic	Antiferromagnetic	Ferromagnetic
2*Integrated spin density	Nonzero, the same magnitude	Zero	Zero	Nonzero
2* Integrated |spin density |	Nonzero, the same magnitude	Zero	Nonzero	Nonzero, larger magnitude

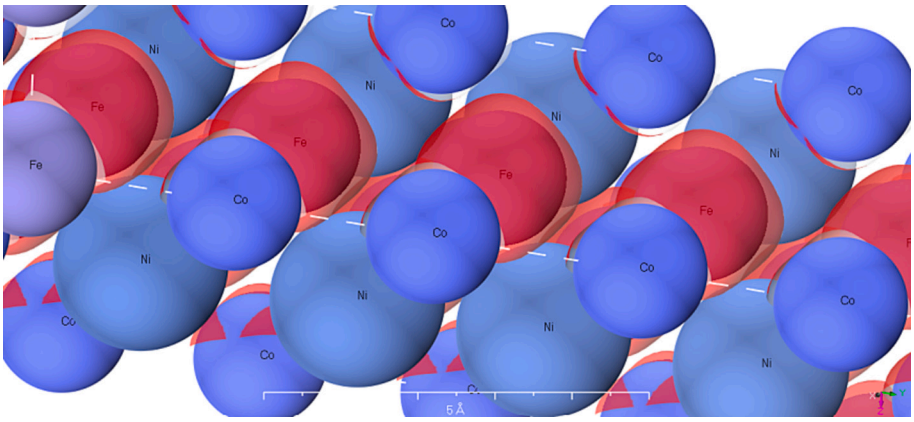

Fig. 9. $Fe_{55}Co_{30}Ni_{15}$ supercell spin density distribution (spin-up: red; spin-down: yellow). (For interpretation of the references to colour in this figure legend, the reader is referred to the web version of this article.)

exhibiting average sizes of 20 nm and 11 nm, respectively. EDX analysis confirmed the material's elemental composition remained consistent throughout the milling process, with minor fluctuations. The magnetic properties of the material indicated soft magnetic behavior, characterized by sigmoidal hysteresis loops and a two-stage evolution of saturation magnetization (Ms) and coercivity (Hc). The multidomain behavior was evident from the remanence (Mr) and squareness ratio (Mr/Ms).

Additionally, computational simulations provided insights into the electronic structure and magnetic properties, revealing ferromagnetic behavior with differences in spin densities and magnetic moment values for the $Fe_{55}Co_{30}Ni_{15}$ alloy.

This study offers a comprehensive understanding of the effects of mechanical alloying on the structural, microstructural, and magnetic characteristics of $Fe_{55}Co_{30}Ni_{15}$ powders. The material displayed favorable soft magnetic properties, making it promising for diverse technical applications.

Author contributions

A. H., S. A., H. F., S. A., K. D., R. B., L. A., W. B, and Y.B. contributed significantly to the conception, design, and execution of the research. They were involved in drafting the manuscript. **J. K. B., M. A. A., K. K. Y., N. E., A. E., and Y.B.** contributed to data analysis, interpretation, and numerical study.

All authors participated in critical revisions and provided important intellectual content.

Funding

The authors extend their appreciation to the Deanship of Scientific Research at King Khalid University, Saudi Arabia, for funding this work through the Research Group Program under Grant No: RGP 2/88/44.

Declaration of Competing Interest

The authors declare that they have no known competing financial

interests or personal relationships that could have appeared to influence the work reported in this paper.

Data availability

No data was used for the research described in the article.

Acknowledgments

The authors extend their appreciation to the Deanship of Scientific Research at King Khalid University, Abha, Kingdom of Saudi Arabia. The authors acknowledge Mr. Foued KHAMMACI from the LM2S Laboratory, Badji Mokhtar Annaba University, for the XRD and SEM measurements.

References

[1] G.S. Reddy, S.R. Sahu, R. Prakash, M. Jagannatham, Synthesis of cobalt-rich alloys with high saturation magnetization: a novel synthetic approach by hydrazine reduction method, Results Phys. 12 (2019) 652–661, https://doi.org/10.1016/j.rinp.2018.12.016.
[2] B. Chitsazan, H. Shokrollahi, A. Behvandi, M. Ghaffari, Magnetic, structural and micro-structural properties of mechanically alloyed nano-structured Fe48Co48V4 powder containing inter-metallic Co3V, J. Magn. Magn. Mater. 323 (2011) 1128–1133, https://doi.org/10.1016/j.jmmm.2010.11.079.
[3] J. Bas, J. Calero, M. Dougan, Sintered soft magnetic materials. Properties and applications, J. Magn. Magn. Mater. 254–255 (2003) 391–398, https://doi.org/10.1016/S0304-8853(02)00934-4.
[4] S.X. Wang, N.X. Sun, M. Yamaguchi, S. Yabukami, Properties of a new soft magnetic material, Nature 407 (2000) 150–151, https://doi.org/10.1038/35025142.
[5] H. Shokrollahi, K. Janghorban, Soft magnetic composite materials (SMCs), J. Mater. Process. Technol. 189 (2007) 1–12, https://doi.org/10.1016/j.jmatprotec.2007.02.034.
[6] Y.K. Yoo, Q. Xue, Y.S. Chu, S. Xu, U. Hangen, H.-C. Lee, W. Stein, X.-D. Xiang, Identification of amorphous phases in the Fe–Ni–co ternary alloy system using continuous phase diagram material chips, Intermetallics. 14 (2006) 241–247, https://doi.org/10.1016/j.intermet.2005.05.013.
[7] K. Chokprasombat, S. Pinitsoontorn, S. Maensiri, Effects of Ni content on nanocrystalline Fe–co–Ni ternary alloys synthesized by a chemical reduction method, J. Magn. Magn. Mater. 405 (2016) 174–180, https://doi.org/10.1016/j.jmmm.2015.12.064.
[8] S.B. Dalavi, J. Theerthagiri, M.M. Raja, R.N. Panda, Synthesis, characterization and magnetic properties of nanocrystalline $Fe_xNi_{80-x}Co_{20}$ ternary alloys, J. Magn. Magn. Mater. 344 (2013) 30–34, https://doi.org/10.1016/j.jmmm.2013.05.026.
[9] N.K. Prasad, V. Kumar, Microstructure and magnetic properties of equiatomic FeNiCo alloy synthesized by mechanical alloying, J. Mater. Sci. Mater. Electron. 26 (2015) 10109–10118, https://doi.org/10.1007/s10854-015-3695-7.
[10] V. Chaudhary, L.P. Tan, V.K. Sharma, R.V. Ramanujan, Accelerated study of magnetic Fe-co-Ni alloys through compositionally graded spark plasma sintered samples, J. Alloys Compd. 869 (2021), 159318, https://doi.org/10.1016/j.jallcom.2021.159318.
[11] C. Toparli, B. Ebin, S. Gürmen, Synthesis, structural and magnetic characterization of soft magnetic nanocrystalline ternary FeNiCo particles, J. Magn. Magn. Mater. 423 (2017) 133–139, https://doi.org/10.1016/j.jmmm.2016.09.005.
[12] Y. Yang, Preparation of Fe-Co-Ni ternary alloys with electro-deposition, Int. J. Electrochem. Sci. 10 (2015) 5164–5175.
[13] M. Beldjehem, S. Alleg, N. Bensebaa, J.J. Sunol, J.-M. Greneche, Thermal stability, structure, hyperfine, and magnetic properties of nanostructured FeCo-2.5wt.%Ni powders, J. Supercond. Nov. Magn. 36 (2023) 301–314, https://doi.org/10.1007/s10948-022-06467-3.
[14] L.G. Betancourt-Cantera, F. Sánchez-De Jesús, A.M. Bolarín-Miró, A. Gallegos-Melgar, J. Mayen, J.A. Betancourt-Cantera, Structural analysis and magnetic characterization of ternary alloys (Co–Fe–Ni) synthesized by mechanical alloying, J. Mater. Res. Technol. 9 (2020) 14969–14978, https://doi.org/10.1016/j.jmrt.2020.10.068.
[15] G.V. Thotakura, A. Rathi, T.V. Jayaraman, Correction to Structure and magnetic properties of mechanically alloyed nanocrystalline Fe-46 at.% Co-34 at.% Ni-20 at.% alloy powder from cryogenic to elevated temperatures (Applied Physics A, (2019), 125, 4, (235), 10.1007/s00339-019-2535-7), Appl. Phys. A Mater. Sci. Process. 125 (2019) 1, https://doi.org/10.1007/s00339-019-2633-6.
[16] H. Raanaei, H. Eskandari, V. Mohammad-Hosseini, Structural and magnetic properties of nanocrystalline Fe–Co–Ni alloy processed by mechanical alloying, J. Magn. Magn. Mater. 398 (2016) 190–195, https://doi.org/10.1016/j.jmmm.2015.09.031.
[17] A. Yakin, T. Simsek, B. Avar, T. Simsek, A.K. Chattopadhyay, A review of soft magnetic properties of mechanically alloyed amorphous and nanocrystalline powders, Emergent Mater. 6 (2023) 453–481, https://doi.org/10.1007/s42247-023-00485-0.
[18] C. Suryanarayana, Mechanical alloying: a novel technique to synthesize advanced materials, Research. 2019 (2019) 1–17, https://doi.org/10.34133/2019/4219812.
[19] N. Dadda, K. Dadda, W. Bouchelaghem, M. Medjaldi, S. Alleg, M. Bououdina, E. K. Hlil, Magnetic and electronic structure studies of nanocrystalline $(Co_2Mn)_{40}Ni_{60}$ alloy, Acta Phys. Pol. A 140 (2021).
[20] T. Şimşek, E. Kavaz, Ö. Güler, T. Şimşek, B. Avar, N. Aslan, G. Almisned, H.M. H. Zakaly, H.O. Tekin, FeCoNiMnCr high-entropy alloys (HEAs): synthesis, structural, magnetic, and nuclear radiation absorption properties, Cer. Inter. 49 (2023) 25364–25370, https://doi.org/10.1016/j.ceramint.2023.05.072.
[21] B. Avar, A.K. Chattopadhyay, T. Simsek, S. Ozcan, B. Kalcan, Synthesis and characterization of amorphous-nanocrystalline Fe70Cr10Nb10B10 powders by mechanical alloying, Appl. Phys. A Mater. Sci. Process. 128 (2022) 537, https://doi.org/10.1007/s00339-022-05680-0.
[22] F. Lemdani, S. Alleg, H. Mechria, N. Saoula, F. Hadj-Larbib, M. Azzaz, Structure and magnetic properties of mechanically alloyed Fe90Al8C2 (wt. %) powders, J. Supercond. Nov. Magn. 36 (2023) 207–215, https://doi.org/10.1007/s10948-022-06456-6.
[23] N. Khitouni, R. Daly, L. Escoda, N. Liorca-Isern, J.J. Sunol, M. Dammak, M. Khitouni, The effect of B and Si additions on the structural and magnetic behavior of Fe-Co-Ni alloy prepared by high-energy mechanical milling, J. Supercond. Nov. Magn. 33 (2020) 2727–2735, https://doi.org/10.1007/s10948-020-05500-7.
[24] T.V. Jayaraman, A. Rathi, G.V. Thotakura, Evaluation of the suitability of $Fe_{40}Co_{30}Ni_{30}$ as a precursor for Fe-rich FeCoNi-based high-entropy semi-hard magnets, Intermetallics. 119 (2020), 106715, https://doi.org/10.1016/j.intermet.2020.106715.
[25] V. Chaudhary, Li Ping Tan, Vinay K. Sharma, R.V. Ramanujan, Accelerated study of magnetic Fe-Co-Ni alloys through compositionally graded spark plasma sintered samples, J. Alloys Compd. 869 (2021), 159318, https://doi.org/10.1016/j.jallcom.2021.159318.
[26] P. Ledwig, M. Kac, A. Kopia, J. Falkus, B. Dubiel, Microstructure and properties of electrodeposited nanocrystalline Ni-Co-Fe coatings, Materials 14 (2021) 3886, https://doi.org/10.3390/ma14143886.
[27] L.G. Verga, C.-K. Skylaris, DFT Modeling of Metallic Nanoparticles, 2018, pp. 239–293, https://doi.org/10.1016/B978-0-08-102232-0.00008-7.
[28] P. Makkar, N.N. Ghosh, A review on the use of DFT for the prediction of the properties of nanomaterials, RSC Adv. 11 (2021) 27897–27924, https://doi.org/10.1039/D1RA04876G.
[29] M. Mamatkulov, I. Yudanov, A. Bukhtiyarov, K. Neyman, Pd single-atom sites on the surface of PdAu nanoparticles: a DFT-based topological search for suitable compositions, Nanomaterials. 11 (2021) 122, https://doi.org/10.3390/nano11010122.
[30] L. Lutterotti, Material Analysis Using Diffraction, Version 2.074. http://www.ing.unitn.it, 2009.
[31] R.A. Young, D.B. Wiles, Profile shape functions in Rietveld refinements, J. Appl. Crystallogr. 15 (1982) 430–438, https://doi.org/10.1107/S002188988201231X.
[32] L. Lutterotti, P. Scardi, P. Maistrelli, LSI - a computer program for simultaneous refinement of material structure and microstructure, J. Appl. Crystallogr. 25 (1992) 459–462, https://doi.org/10.1107/S0021889892001122.
[33] M.D. Segall, P.J.D. Lindan, M.J. Probert, C.J. Pickard, P.J. Hasnip, S.J. Clark, M. C. Payne, First-principles simulation: ideas, illustrations and the CASTEP code, J. Phys. Condens. Matter 14 (2002) 2717–2744, https://doi.org/10.1088/0953-8984/14/11/301.
[34] J. Kohanoff, Electronic Structure Calculations for Solids and Molecules, Cambridge University Press, 2006, https://doi.org/10.1017/CBO9780511755613.
[35] W. Kohn, L.J. Sham, Self-consistent equations including exchange and correlation effects, Phys. Rev. 140 (1965) A1133–A1138, https://doi.org/10.1103/PhysRev.140.A1133.
[36] J.P. Perdew, K. Burke, M. Ernzerhof, Generalized gradient approximation made simple, Phys. Rev. Lett. 77 (1996) 3865–3868, https://doi.org/10.1103/PhysRevLett.77.3865.
[37] D.M. Ceperley, B.J. Alder, Ground state of the electron gas by a stochastic method, Phys. Rev. Lett. 45 (1980) 566–569, https://doi.org/10.1103/PhysRevLett.45.566.
[38] H.J. Monkhorst, J.D. Pack, Special points for Brillouin-zone integrations, Phys. Rev. B 13 (1976) 5188–5192, https://doi.org/10.1103/PhysRevB.13.5188.
[39] Mol L. Lu, Mechanical Alloying, Kluwer Acad. Publ, Massachusetts, 1998.
[40] S. Alleg, A. Bekhouche, H. Hachache, J.J. Sunol, Effect of aluminum addition on the microstructure, magnetic, and mechanical properties of FeCrCoNiMn high-entropy alloy, Crystals 13 (10) (2023) 1483, https://doi.org/10.3390/cryst13101483.
[41] M.R. Nikkhah, K. Gheisari, Effect of Co addition on the structural evolution and magnetic properties of Nanocrystalline Fe50Ni50-xCox alloys prepared by mechanical alloying, J. Supercond. Nov. Magn. 36 (2023) 315–325, https://doi.org/10.1007/s10948-022-06471-7.
[42] G.K. Williamson, R.E. Smallman III, Dislocation densities in some annealed and cold-worked metals from measurements on the X-ray debye-scherrer spectrum, Philosoph. Magaz. A J. Theo. Exp. Appl. Phys. 1 (1) (1956) 34–46, https://doi.org/10.1080/14786435608238074.
[43] H.J. Fecht, Nanostructure formation by mechanical attrition, Nanostruct. Mater. 6 (1995) 33–42, https://doi.org/10.1016/0965-9773(95)00027-5.
[44] H. Moumeni, A. Nemamcha, S. Alleg, J.M. Grenèche, Stacking faults and structure analysis of ball-milled Fe50%Co powders, Mater. Chem. Phys. 122 (2–3) (2010) 439–443, https://doi.org/10.1016/j.matchemphys.2010.03.020.
[45] T. Khelfa, M. Mhadhbi, N. Khitouni, T. Bachaga, J.J. Sunol, M. Khitouni, Effect of high-energy ball milling on the structural and magnetic behavior of $Fe_{60}Al_{40}$ alloy, J. Mater. Eng. Perform. (2023) 1–11, https://doi.org/10.1007/s11665-023-08438-8.

[46] A. Yakın, T. Şimşek, B. Avar, et al., The effect of Cr and Nb addition on the structural, morphological, and magnetic properties of the mechanically alloyed high entropy FeCoNi alloys, Appl. Phys. A Mater. Sci. Process. 128 (2022) 686, https://doi.org/10.1007/s00339-022-05836-y.
[47] R. Daly, N. Khitouni, M.L. Escoda, N.L. Isern, J.J. Sunol, J.M. Greneche, M. Khitouni, Microstructure, magnetic and Mössbauer studies of mechanically alloyed FeCoNi nanocrystalline powders, Arab. J. Sci. Eng. 46 (2021) 5633–5643, https://doi.org/10.1007/s13369-020-05166-2.
[48] D. Yuping, Z. Yahong, W. Tongmin, G. Shuchao, L. Xin, L. Xingjun, Evolution study of microstructure and electromagnetic behaviors of Fe–Co–Ni alloy with mechanical alloying, Mater. Sci. Eng. B 185 (2014) 86–93, https://doi.org/10.1016/j.mseb.2014.02.014.
[49] S. Azzaza, S. Alleg, H. Moumeni, A.R. Nemamcha, J.L. Rehspringer, J.M. Greneche, Magnetic properties of nanostructured ball-milled Fe and $Fe_{50}Co_{50}$ alloy, J. Phys. Condens. Matter 18 (2006) 7257, https://doi.org/10.1088/0953-8984/18/31/020.
[50] G. Herzer, The random anisotropy model: a critical review and update, in: Properties and Applications of Nanocrystalline Alloys from Amorphous Precursors. NATO Science Series 184, Springer, Dordrecht, 2005, pp. 15–34, https://doi.org/10.1007/1-4020-2965-9_2.
[51] F. Nejadsattari, Z.M. Stadnik, J. Przewoźnik, B. Grushko, Mössbauer spectroscopy, magnetic, and ab-initio study of the approximant Al76Ni9Fe15 to a decagonal Al–Ni–Fe quasicrystal, J. Alloys Compd. 662 (2016) 612–620, https://doi.org/10.1016/j.jallcom.2015.12.115.